1	
2	Design and performance of Fe3O4@ SiO2/MoO3/polydopamine-
3	graphene oxide composites for visible light photocatalysis
4 5 6 7	Rheamay Vasallo-Antonio,¹ Janire Peña-Bahamonde,² Mariano D. Susman,³ Florencio C. Ballesteros Jr,¹ and Debora F. Rodrigues²
8	¹ Environmental Engineering Program, Department of Chemical Engineering,
9	University of the Philippines, 1101 Diliman, Quezon City, Philippines
10	² Department of Civil and Environmental Engineering, University of Houston,
11	Houston, TX, USA
12	³ Department of Chemical and Biomolecular Engineering, University of Houston,
13	4726 Calhoun Road, Houston, TX, 77204, USA
14	
15	* Corresponding Author: Debora F. Rodrigues, email: <u>dfrigirodrigues@uh.edu</u>
16	
17	

Abstract

18

19

20

21

22

23

24

25

26

27

28

29

30

31

32

33

34

35

36

Photocatalysis is a well-known low-cost approach for the degradation of pollutants utilizing the energy of light. However, most studied photocatalysts are characterized by wide bandgaps (TiO₂, ZnO, Cu₂O), restricting the solar light utilization to UV. In this study, a magnetic composite catalyst comprised of Fe₃O₄@SiO₂ core-shell nanoparticles, which allow the magnetic recovery and recycling of the catalyst, combined with catalytically active MoO₃ particles dispersed in a polydopaminegraphene oxide (GO) matrix, was synthesized to improve visible light removal of methylene blue and phenol. The multicomponent nanocomposite composition was optimized by response surface methodology using second-order polynomials to maximize the adsorption and photocatalytic removals, using initially methylene blue (MB) as model pollutant. High coefficients of determination (R^2) of 0.84 and 0.94 were obtained for adsorption and photocatalysis, respectively. The catalyst was characterized by various techniques and the effects of the photocatalyst dosage, initial MB concentration, light source, and pH were investigated, achieving a 99.2 % MB removal with up to two rounds of recycle. The nanocomposite also demonstrated to produce ca. 60% H₂O₂ and attain a 85% phenol degradation in the presence of H₂O₂. Furthermore, it was established that both phenol and MB degradation mechanisms by the new nanocomposite involve the production of reactive oxygen species.

37

38

39

Keywords: Photocatalysis, adsorption, response surface methodology, Graphene oxide, Phenol removal, methylene blue removal.

40

41

1. Introduction

43

44

45

46

47

48

49

50

51

52

53

54

55

56

57

58

59

60

61

62

63

64

65

66

The declining availability of traditional groundwater supplies, increasing contamination of surface water, as well as the growing human demand for clean water call for novel approaches to effectively remove water pollutants. Furthermore, several emerging pollutants are not susceptible to biological treatments as they exhibit high chemical stability and/or great difficulty to be completely mineralized [1]. For these reasons, advanced oxidation processes (AOPs), which have the capability to completely degrade organic or convert them into less toxic compounds, are very desirable. AOPs, and specifically photocatalysis, have been extensively studied for the degradation of organic pollutants for water and wastewater treatment. The effectiveness of several nanomaterials in the removal of organic compounds in water has been proven in previous studies [2–5]. Additional studies on organic matter removal using hybrid treatment technologies are needed without leaving behind harmful toxic by-products. Photocatalysis has been widely employed as a cost-effective and efficient alternative to clean water and for environmental remediation. This technique combines a heterogeneous catalyst and UV-Vis light to oxidize organic pollutants. A group of primary light absorbent semiconductors was explored as photocatalysts as early as in the 1970s [6]. For instance, titanium dioxide (TiO₂) was reported as one of the most efficient catalysts [7]; however, its large band-gap limits its use under visible light. Utilizing nanomaterials that

can perform under sunlight was reported as a promising method to further

improve photocatalytic treatment [8].

The development of photocatalysts with enhanced properties, such as visible light photocatalytic activity, reusability and stability, is essential for practical applications. The synthesis of graphene-based semiconductor nanocomposites to further improve the photocatalytic efficiency of different nanomaterials has been previously proposed but has not been systematically investigated.[9-14] Furthermore, most prior studies incorporated wide bandgap semiconductors into graphene or graphene oxide nanomaterials [15,16]. For example, the degradation of different organic molecules and photocatalytic inactivation of microorganisms have been previously reported with different graphene oxide based metal oxide nanocomposites, such as Magnetic ZnFe₂O₄nanocomposites, ZnO/graphene-oxide, Ag/TiO₂ and graphene TiO₂/graphene nanocomposites, and Ag₃PO₄-Graphene composites, among others, [14,17,18]. In the present study, we will systematically investigate the incorporation of MoO₃ in graphane oxide since graphene and graphene oxide have been shown to have high adsorption capability [19], while MoO₃ nanomaterials have shown excellent photocatalytic activity under visible light [20-23]. Regardless of the use of visible light, when designing photocatalysts, other factors should also be considered, i.e. dissolution and reusability since lifetime and potential reusability of nanomaterials will limit its applicability. For example, it has been suggested that some of the metal oxide nanoparticles exhibit some instability in water and can release ions in the environment causing harmful effects. [24] This is also the case for MoO₃, which has also shown to dissolve at pH 7 in water [25][26]. Hence, the need of a very systematic approach to optimize a visible light nanocomposite, such as MoO₃, that is stable in normal water treatment conditions.

67

68

69

70

71

72

73

74

75

76

77

78

79

80

81

82

83

84

85

86

87

88

89

Herein, an enhanced photocatalyst utilizing the magnetic properties of a Fe₃O₄ particles protected by a SiO₂ shell, and the photocatalytic properties of MoO₃ dispersed in a GO-polydopamine matrix was developed. We hypothesized that this combination would lead to a multifunctional material that can be easily recovered, be able to remove organic compounds, and possess an improved photo-reactivity under visible light. However, to achieve the maximum removal potential of the nanocomposite, it is crucial to optimize the ratio of the different nanomaterial components. Thus, an approach based on the response surface methodology (RSM) [27,28] was undertaken to design this multifunctional material. Box-Behnken design (BBD), which is reported as a more economical design than others, was selected because it requires fewer number of experiments while still providing an excellent output prediction [29]. Linear regression analysis was employed to predict the responses and was compared to the actual experimental values. Furthermore, the fitness of the models was tested using analysis of variance (ANOVA). Once the optimum ratio of components was identified, experiments using the optimized photocatalyst were performed to validate the model's predictions. The optimization of the photacalysis of this new material via percent removal was evaluated by analyzing the methylene blue discoloration, since this dye is very easy to monitor by UV-Vis. However, to consider its potential applicability, we also investigated phenol removal. As of today, very few studies have evaluted the application of visible light photocatalysts in environmental contaminants, such as phenol with magnetic MoO₃-graphene oxide nanocomposites. Here, we investigated a novel magnetic MoO₃-graphene oxide nanocomposite for the removal of phenol as well as its potential reusability.

92

93

94

95

96

97

98

99

100

101

102

103

104

105

106

107

108

109

110

111

112

113

114

115

117 2. Experimental section

powder 118 2.1. Materials. Graphite (<45 μm), NaNO₃, KMnO₄, 119 (NH₄)₆Mo₇O₂₄·4H₂O, FeCl₂·4H₂O, FeCl₃·6H₂O, methylene blue (MB), phenol, 120 p-benzoquinone (p-BQ), ethanol, isopropyl alcohol (IPA), triethanolamine (TEOA), 121 and Tris buffer solution were purchased from Sigma-Aldrich. Dopamine 122 hydrochloride (D-HCl), tetraethyl orthosilicate (TEOS), H₂SO₄, HNO₃, HCl, 30 123 % H₂O₂, 28 wt% NH₄OH, glutathione and 5,5'-dithiobis(2-nitrobenzoic acid) 124 (Ellman's reagent) were supplied by Fisher Scientific. All reagents were used 125 as received. Aqueous solutions were prepared using deionized (DI) water 126 (≥18.2 MΩ). 127 2.1.1. Synthesis of Fe₃O₄ nanoparticles. Magnetic Fe₃O₄ particles were 128 produced by a co-precipitation method. Briefly, in a round bottom flask, 16.0 129 mL of 1.0 M FeCl₃·6H₂O and 4.0 mL of 2.0 M FeCl₂·4H₂O, both in 2.0 M HCl, 130 were added and magnetically stirred. While stirring, 300 mL of 1.0 M NH₄OH 131 was added at once immediately forming a black Fe₃O₄ precipitate. The reaction 132 was performed under Ar atmosphere. Precipitates were magnetically collected 133 exposing the suspension to a strong magnetic field (N52 Neodymium 2-inch 134 cube magnet, Applied Magnets), and purified resuspending and washing the 135 material with DI water until pH 7 was reached, after which it was freeze-dried 136 for 24 h. 137 2.1.2. Synthesis of Fe₃O₄@SiO₂. The SiO₂ shell was prepared using a 138 modified Stöber method [30,31] Fe₃O₄ particles (100 mg) were dispersed by 139 sonication in 50 mL ethanol/water (4:1) and 1.20 mL of 28 wt% NH₄OH for 1 140 h. Then, 0.35 mL TEOS was added dropwise and stirred for 2 h (note the magnetic bar did not attract particles due to its low magnetic field). The 141

- resulting black product was collected magnetically, washed with DI water until
- pH 7, and freeze-dried.
- 2.1.3. Synthesis of MoO₃. Molybdenum trioxide (MoO₃) was synthesized by a
- solution-based self-assembly route [32] with some modifications. Briefly, 12.3
- 146 g of (NH₄)₆Mo₇O₂₄·4H₂O and 80.0 mL DI water were stirred at room
- 147 temperature in a 125 mL round bottom flask. Then, 2 M HNO₃ was added
- dropwise until a pH of ca. 1 was reached, and the mixture was stirred (400 rpm)
- in an oil bath at 90 °C for 8 h. The resulting white powder was isolated by
- 150 centrifugation and washed with DI water until pH 7, and then the suspension
- was freeze-dried.
- 2.1.4. Synthesis of GO. Graphene oxide (GO) synthesis was carried out using
- the Hummers method with some modifications [33] as follows: 2.0 g of
- graphite powder and 92.0 mL of concentrated H₂SO₄ were magnetically stirred
- in an ice bath at 150 rpm for 20 min. Then, 2.0 g NaNO₃ was added and the
- stirring continued for another hour. The system was then placed in an oil bath at
- 157 35 °C and 12.0 g of KMnO₄ was added slowly. After stirring for 16 h, 160 mL
- 158 DI water were added, the temperature was further increased to 90 °C and
- stirring was continued for another 30 min. Next, a solution containing 360 mL
- DI water and 40 mL H₂O₂ (30 %) was added slowly. Then, the mixture was
- 161 cooled down, the solid was purified by centrifugation several times with DI
- water until pH 7. The brown precipitate was dispersed in 2.0 L DI water and
- subsequently sonicated using a tip sonicator for 8 h to exfoliate the GO. The
- 164 GO suspension was freeze-dried to obtain the GO powder.
- 2.1.5. Synthesis of Fe₃O₄@SiO₂/MoO₃ (FSM). FSM nanocomposites were
- prepared by a co-deposition method. As prepared Fe₃O₄@SiO₂ (10 mg) were

dispersed in 20.0 mL 10 mM Tris buffer solution of pH 8.5, and sonicated for 5 min. Different weights of D-HCl and MoO₃, as described in the response surface methodology (RSM) experimental design (*vide infra*), were added (Table S1). Then, the mixtures were sonicated again for 5 min and stirred for 24 h. The resulting products were magnetically collected and freeze-dried for 24 h.

2.1.6. Synthesis of Fe₃O₄@SiO₂/MoO₃/PDA-GO (FSM-GO) composites.

FSM-GO composites were prepared by a co-deposition method. Each FSM material was dispersed in 20.0 mL 10 mM Tris buffer solution (pH = 8.5) by sonication for 5 min. D-HCl and GO were added and sonicated with the previous suspension for 5 min. The added GO and D-HCl amounts were varied as described in Table S1. Subsequently, the mixture was stirred for 24 h at 40 °C. The resulting black composite was magnetically collected, washed with DI

water until pH 7, and then freeze-dried.

3. Materials characterizations. Powder X-ray diffraction (XRD) was performed in a Philips X'pert Pro X-ray diffractometer, using the Cu K α radiation (λ = 1.54 Å) and scanning 2 θ from 5 to 80 ° at a rate of 0.02 °/sec. The voltage employed was 40 kV and the current intensity was 40 mA. The morphology of the nanomaterials was examined by scanning electron microscopy (SEM) in a LEO FEI 1525 SEM instrument equipped with an Inlens detector and using a working distance of 3–4 mm and an accelerating voltage of 8 kV. For the Fourier transform infrared (FTIR) spectroscopy, a Nicolet iS50 spectrometer with diamond plate, was used. Omnic 8 Software (Thermo Fisher Scientific, USA) was used to process the FTIR data. Raman

spectroscopy was carried out using a HORIBA iHR320 Spectrometer equipped with a Synapse CCD with a laser at 532 nm. Energy dispersion spectroscopy (EDS) was performed in a JEOL SM-31010/METEK EDAX system at 15 kV and a 15 mm working distance. For the MoO₃ bandgap energy (E_g), a Hitachi UV-Vis Spectrophotometer U-2001 in reflectance mode was used to determine the absorption edge (A = 420 nm) and the bandgap was calculated using equation 1.

198

192

193

194

195

196

197

199
$$\lambda \text{ (nm)} = 1240 \text{ (eV/nm)}/E_g$$
 (1)

200

- For the FSM-GO bandgap energy evaluation, the reflectance was very weak.
- For this reason, the absorbance mode and the Tauc relation (equation 2) were
- 203 used [34];

204

$$\epsilon h v = C(h v - E_g)^r \tag{2}$$

- where ε is the absorption coefficient, hv is the energy of the incident photons,
- and r is an exponential factor. The result for the direct bandgap measurement
- with $r = \frac{1}{2}$ is presented as a Tauc plot. Origin Pro 8 software (OriginLab,
- Northampton, MA) was used for the data analysis.
- 3.1. Photocatalytic experiments. The removal of a model organic compound,
- 212 methylene blue (MB), was investigated under visible light. The magnetic
- 213 photocatalyst (4.0 mg) was added to the MB solution (20.0 mL, 40.0 mg
- MB/mL, pH 5) and the suspension was magnetically stirred in the dark for 30
- 215 min to achieve adsorption equilibrium by covering the vial with aluminium foil
- 216 [35]. Then, it was exposed to visible light for photocatalytic reactions, which

were carried out in a box reactor (24 cm in width, 35 cm in length) with a removable window at the top where the lamps (4W, 4 units Philips cool white lamps) were attached for illumination. For the light-emitting diode (LED) as light source, as previously described [36], the photocatalytic experiments were carried out using instead a 2 m flexible LED strip (SMD 5050, 30 pcs/m, 7.5 W/m). Lamp spectra are shown in Figure S1. The suspensions were stirred under illumination for 3 h at 180 rpm, withdrawing aliquots (200 μ L) every 20 min, and magnetically separating the catalyst from the solution, which was transferred to a 96-well microtiter plate. The removal of MB was monitored by measuring the absorbance in a UV–Vis spectrophotometer (Biotek, Synergy Mx Microtiter plate reader, USA) at 665 nm (ϵ = 82,000 M·cm⁻¹) [37]. The % MB removal was reported according to equation (3),

$$\% Removal = \frac{C_0 - C_t}{C_0} \times 100 \tag{3}$$

where C_0 and C_t are the initial and final MB concentrations, respectively. A blank containing only MB, but excluding the catalyst, and a control containing the nanoparticles and MB solution, but excluding light exposure (adsorption only), were also prepared. Control experiments were carried out with the corresponding weight amount of each material in the final nanocomposite. All experiments were carried out in triplicates. When photocatalysis was performed at different pHs, the pH was adjusted either with NaOH or HCl. Removal of phenol was also investigated by suspending FSM-GO (20.0 mg) in an aqueous phenol solution (20.0 ml, 20.0 mg/L, pH 5). As a blank, the same amounts of phenol solution and photocatalyst with 20 μL of H₂O₂ were tested. The photocatalyst suspension was magnetically stirred in the dark for 1 h to achieve adsorption equilibrium [2], and subsequently exposed to Vis light using

LED lights. Photocatalytic experiments were carried out in a box reactor, as previously described. The suspension was magnetically stirred at 180 rpm during irradiation. One mL aliquots were taken using a plastic syringe every 3 h and the catalyst magnetically collected. Solutions were analysed by highperformance liquid chromatography (HPLC) in an Agilent Technologies 1200 series instrument with an Eclipse XDB-C18 chromatographic column (5 µm × 150 mm × 460 mm). A mixture of (A) 95 v% DI water, 5 v% acetonitrile, 0.1 v% formic acid, and (B) 100 % methanol, 0.1 % formic acid, in a 33:67 A:B volume ratio was used as mobile phase at a 0.5 mL/min flow rate with an injection volume of 5.0 µL. A calibration curve was generated using phenol standards of up to 20 ppm. In the nanocomposite, while GO adsorbed MB, MoO3 was responsible for the photocatalytic activity of the sample. To quantify the amount of dye that has been photodegraded, we made some distinctions between adsorption and photocatalysis degradation. Adsorption was determined by experiments performed under dark conditions. The photocatalytic activity of MoO₃ was calculated by subtracting the discoloration results of MB at the end of the reaction of both light and dark experiments. 3.2. Statistical analysis and compositional optimization. To optimize the adsorption and photocatalytic efficiencies in the removal of MB, a three-factor and five-level Box-Behken design (BBD) was performed using Design Expert 11.0 software from Stat-Ease Inc. (Minneapolis, USA). We used as independent factors the total weights of $MoO_3(x_1)$, $GO(x_2)$, and D-HCl (x_3) to create 17 randomized design points. Adsorption (Y_{ads}) and photocatalytic removal ($Y_{photocat}$) were the responses evaluated, as reported in Table S1.

241

242

243

244

245

246

247

248

249

250

251

252

253

254

255

256

257

258

259

260

261

262

263

264

Based on the successful synthesis of the composites, preliminary investigations were performed to determine the range of levels for the independent factors.

The obtained responses were fitted by second-order polynomials (equation 3) to establish the mathematical relationships with the *a priori* independent variables:

$$Y = B_o + \sum_{i=1}^{n} B_i x_i + \sum_{i=1}^{n-1} \sum_{j=i+1}^{n} B_{ij} x_i x_j + \sum_{i=1}^{n} B_{ii} x_i^2$$
 (3)

- where B_o are constant offset coefficients; B_i , B_{ij} and B_{ii} are coefficients for linear interactions and quadratic effects, respectively; n is the number of independent variables, and x_i , x_j are the independent variables.
- To evaluate the significance of each term, analysis of variance (ANOVA) was performed with $p \le 0.05$. The quality and adequacy of the fitted models were evaluated by the coefficient of determination (R^2) , lack of fit criterion, Fisher test (F-value), and residual diagnostics. Furthermore, to validate the response models, additional confirmation tests were performed.
- Statistical compositional optimizations, such as numerical optimization, residual analysis, and surface analysis, were performed.
- 3.3. Scavengers experiments. Photocatalysis experiments were performed under the same conditions as described in section 3.1; however, to each reaction mixture the scavengers at 10 mM TEOA, 75 mM IPA or 1 mM p-BQ were included in order to evaluate the photocatalytic degradation mechanism.
- 3.4. Reactive oxygen species (ROS) assay. The production of ROS was estimated via the Ellman's assay, which quantifies the oxidation of thiol groups of glutathione (GSH) [26,38–40]. Briefly, 225 μL of an aqueous suspension

(200 mg sample /L) were mixed with 225 μ L of a 0.4 mM GSH solution in 50 mM NaHCO₃ buffer pH = 8.6. Mixtures were stirred during 2 h, under light and dark conditions. GSH fully oxidized with H2O2 and GSH without added material were used as positive and negative controls, respectively. Then, 20 µL of Ellman's reagent (100 mM) was introduced into each tube, allowed to react for 10 min, and the nanostructures were removed by filtration using a 0.2 µm syringe filter (Corning, U.S.A.). A spectrophotometric quantitation was perfored by measuring the absorbance at 412 nm (Biotek, Synergy Mx Microtiter plate reader, USA) and calculating the GSH loss % by GSH loss = $(A_{nc}-A_s)/A_{nc}$, where A_{nc} and A_s represent the absorbances of the negative control and the sample, respectively. Control experiments were carried out with the corresponding weight amount of each material in the final nanocomposite. All samples were measured in triplicates. 3.5. MoO₃ dissolution test. A previous study reported dissolution of MoO₃ at neutral pH may occur [26]; thus, the stability/dissolution of the optimized FSM-GO sample was evaluated. Dissolution of about 200 mg/L FSM-GO in DI H₂O was tested at pH values 5 and 7, as confirmed using a pH meter (HORIBA Model D-21). The pH was adjusted adding either HCl or NaOH. After 24 h, the nanomaterial was magnetically separated and the supernatant was centrifuged with Amicon ultrafiltration devices (30,000 NMWL) to ensure the complete removal of the nanomaterial followed by atomic absorption spectrometry (AAS) analysis using an AAnalyst 200 spectrometer (Perkin Elmer). A calibration regression was produced with standard solutions with concentrations between 0 to 40 ppm. Results were reported for triplicate measurements, in mg/L. Nitrous oxide

289

290

291

292

293

294

295

296

297

298

299

300

301

302

303

304

305

306

307

308

309

310

311

- 313 with flow rate of 3.3 L/min and acetylene at 2.5 L/min were used as flame
- 314 oxidants.
- 315 3.6. Reusability. Photocatalytic experiments were performed using the
- 316 optimum operating parameters (vide infra) obtained from the parametric study.
- 317 After every photocatalytic measurement the catalyst was magnetically
- separated, washed once with DI water, freeze-dried, and reutilized for the next
- 319 photocalytic cycle.

320

321

4. Results and Discussion

- 322 The use of composites opens the possibility of designing multi-functional
- 323 materials with properties suitable for targeted applications. In this case, we
- have combined the Fe₃O₄@SiO₂ magnetic properties with the MoO₃ catalytic
- 325 properties, and enhanced adsorption and visible light absorption by adding GO
- 326 to produce a material with improved catalytic properties and reusability.
- 327 4.1 Response surface methodology (RSM) for the design of the new
- 328 nanocomposite. RSM was used to determine the best amount of each
- 329 component in the nanocomposite, as well as the role of the different
- 330 components of the nanocomposite in adsorption and photocatalysis. The
- 331 different weighted amounts of MoO₃ (x_1), GO (x_2), and dopamine
- 332 hydrochloride (D-HCl, x_3) used in the synthesis were optimized by BBD. Table
- 333 S1 presents all the removal responses experimentally obtained for the MB
- removal experiments, which were used to fit the model described by Equation
- 335 3. The resulting expressions for the predicted adsorption and photocatalysis
- responses are presented by equations 7 and 8 below.

 $Y_{\text{ads}} = 41.24 - 0.79x_1 + 15.65x_2 - 11.65x_3 + 0.65x_1x_2 + 10.5x_1x_3 - 0.65x_1x_2 + 10.5x_1x_3 - 0.65x_1x_2 + 10.5x_1x_3 - 0.65x_1x_2 + 0.65x_1x_2 + 0.65x_1x_3 + 0.65x_1x_2 + 0.65x_1x_3 + 0.65x_1x_2 + 0.65x_1x_3 + 0.65x_1x_3$

$$339 9.42x_2x_3 + 7.97x_1^2 - 11.22x_2^2 + 2.69x_3^2 (7)$$

 $340 \quad Y_{photocat} = 51.01 + 6.45x_1 + 19.30x_2 - 18.07x_3 - 7.05x_1x_2 + 0.88x_1x_3 - 7.05x_1x_3 - 7.05x_1$

$$341 \quad 3.16x_2x_3 + 0.62x_1^2 - 7.37x_2^2 + 12.84x_3^2 \tag{8}$$

- The absolute values of the coefficients in the modelled response equations denote the nature of how each factor (or their interaction) influences the removal [41]. Positive and negative coefficients imply improved and inhibited responses, respectively [42].
- Only the amount of GO (x_2) had a positive effect on MB adsorption (equation 7), considering the signs of the first order terms. Previous investigations [29,43–47] reported that GO concentration has a large effect on the adsorption removal of diverse pollutants in hybrid materials. Similarly, the amount of GO and MoO₃ (x_1) had a positive effect on MB removal (equation 8). Coefficient and constant terms with higher values in equation 8 suggests that photocatalysis will exhibit higher removals compared to adsorption, as shown in Table S1.
- The obtained results confirmed that GO plays a major role in the adsorption, which is a very important initial stage of the photocatalytic process. Analysis of variance (ANOVA) for the quadratic models (Tables S2 and S3) were evaluated to confirm the significance of the effect of each dependent variable through F-test and probability p-value. The terms of the model are significant if p-values are < 0.05.
- The regression model *F*-values for adsorption was 4.04 and for photocatalysis was 13.24. The obtained *p*-values for both models were less than

0.05. They were 0.039 for adsorption and 0.001 for photocatalysis, suggesting that the models are considered to be statistically significant. Both models showed relatively high R^2 of 0.84 and 0.94 for adsorption and photocatalysis, respectively. Better predictability is demonstrated by R^2 values close to 1 [48] indicating that the predicted and experimental values exhibited a good correlation [29,47].

The model reduction was performed to improve the reliability and accuracy of the model; non-significant terms according to ANOVA were removed from the quadratic models (equations 9 and 10).

$$Y_{ads(2)} = 43.18 + 12.98x_2 - 9.56x_3 \tag{9}$$

$$Y_{photocat(2)} = 39.55 + 4.05 x_1 + 8.72 x_2 - 7.55 x_3$$
 375 (10)

It can be observed that adsorption and photocatalysis are mainly affected by the linear terms and not by the quadratic and interaction terms. After model reduction, the models became highly significant with increased F-values of 12.18 and 23.48 and decreased p-values of 0.0013 to < 0.0001 for adsorption and photocatalysis, respectively. ANOVA for the reduced model for both adsorption and photocatalysis, are shown in Table S4 and Table S5, respectively. Furthermore, the adequate precision values, which are defined as the signal-to-noise ratio of the models, were generated to compare the predicted responses and predicted errors. A value > 4 is desired, indicating adequate signal [48]; predicted values by the model, 8.76 and 13.25 for adsorption and for photocatalysis, respectively, justify that the predicting responses were

acceptable. Comparing the generated results of the entire criterion considered, both models for adsorption and photocatalysis were significant. It can be noted, however, that the model obtained for photocatalysis is more reliable and accurate compared to that of the adsorption.

The accuracy of the data and the models were analysed by the distribution of the residuals, where the distributed points should follow straight lines. This analysis was performed using the Design Expert Software. The difference between the actual responses and the responses predicted by the models are defined as the residuals. Normal probability plots of residual values are shown in Figure S2. Adsortion and photocatalysis responses (Figure S2a and Figure S2b) show that the data closely followed straight lines. The random scatter of the residuals indicates that the data are normally distributed, and no response transformations are needed. Good normality plots can be observed.

The correlations between actual experimental and predicted responses (Figure S2c for adsorption S2d for photocatalysis) are both approximately linear. The reduced models show that there is a good correlation between actual experimental responses and predicted responses.

The responses obtained by RSM were used to analyse the individual and combined effects of the input variables [47]. The combination of adsorption and photocatalysis surface plots is shown in Figure S3. The combined effect of the MoO₃ and GO amounts on the MB adsorption, keeping D-HCl at the lowest range, is shown in Figure S3a. An increase in % MB removal is observed when the amount of GO is the highest, which may result from the presence of more functional groups capable of adsorbing MB. It was reported [29,47,49] that the hydroxyl group present on the GO surface plays a significant role in the

removal of contaminants. This observation is consistent with the presence of hydroxyl groups in these composites, as demonstrated by FTIR measurements. Figure S3b illustrates the combined effects of the D-HCl and GO amounts, at a constant level of MoO3 in the middle range. An increased MB removal is observed when GO is increased, while keeping the D-HCl at the lowest range. On the other hand, Figure S3c shows the effect of D-HCl and MoO₃ on the % MB removal keeping the amount of GO at the highest range. An increase in the % MB removal can be observed when the level of D-HCl was kept at the lowest range and MoO₃ at the middle range. In the case of photocatalysis, Figure S3d shows the effect of the amount of GO and MoO₃ on the % MB removal, while keeping the D-HCl amount at the lowest range. % MB removal increases when both GO and MoO3 levels increase. This trend is opposite to that of % MB adsorption and can be explained by the difference in the mechanism. We conclude that the introduction of more GO resulted in a higher adsorption capacity, while the addition of MoO₃ into the nanocomposite resulted in furthering the degradation of the adsorbed MB. Both GO and MoO₃ positively influenced the photocatalysis.

413

414

415

416

417

418

419

420

421

422

423

424

425

426

427

428

429

430

431

432

433

434

435

436

437

Considering the combined effect of D-HCl and GO on the % MB removal for photocatalysis (Figure S3e), an increase in the % MB removal for adsorption was obtained when GO was kept in the highest considered range and D-HCl on the lowest range. Finally, the trend between D-HCl and MoO₃ is further observed when D-HCl was kept in the lowest range and MoO₃ in the middle range. Positive x_1 was observed in the generated model equation suggesting the positive influence of MoO₃ in % MB removal for photocatalysis. To summarize, it can be concluded from the surface plot analizes that % MB

removals for both adsorption and photocatalysis are most favourable when the amount of GO was kept in the highest range, the amount of MoO₃ at the lower-middle range and the D-HCl at the lowest considered range.

4.2 Optimization and validation. To choose a response with the highest desirability, the desirability function of RSM was used to perform the optimization of the nanocomposites. The adsorption and photocatalysis experiments to validate the model were performed with the FSM-GO nanocomposites prepared using the optimum composition determined by the photocatalytic model. The optimization determined that 25 mg of GO, 10 mg of MoO_3 was, and 5 mg of D-HCl were the optimal amounts. The predicted removals using the reduced equations for both adsorption and photocatalysis were 65.72 and 83.70%, respectively, with the desirability of 0.94. Figure 1 shows the results for the optimum FSM-GO formulation. Two-tailed *t*-test analysis at $\alpha = 0.05$ was performed. Calculated *p*-values of 0.061 and 0.075 for adsorption and photocatalysis were obtained. The results confirm that there is no statistical difference between the predicted and actual removals.

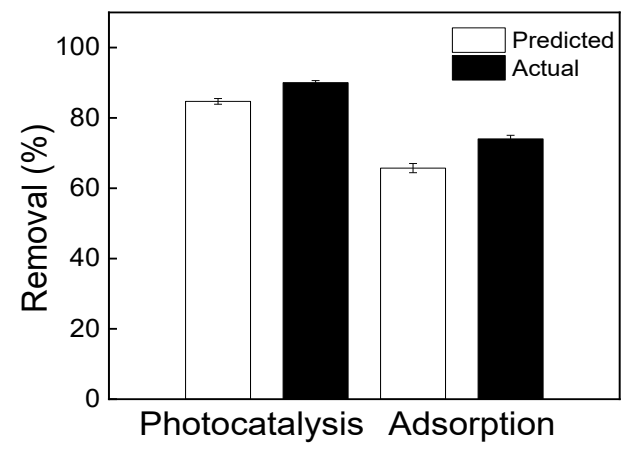


Figure 1. Predicted and actual removals for photocatalysis and adsorption with optimized FSM-GO. Standard deviations are represented by error bars.

4.3 Catalyst preparation and characterization. The preparation of the composite magnetic catalyst comprises the synthesis of the individual components and their stepwise combination, i.e., first, the synthesis of Fe₃O₄@SiO₂ by a well-established Stöber method [30,31], as well as of GO and MoO₃ components; second, the Fe₃O₄@SiO₂/MoO₃ (FSM) co-deposition; and third, the dopamine polymerization in presence of FSM and GO to yield the final FSM-GO material. Each of these materials were characterized to ensure successful synthesis.

457

458

459

460

461

462

463

464

465

466

467

468

469

470

471

472

473

474

475

476

477

478

479

480

The FTIR spectrum of Fe₃O₄ (Figure 2a) exhibits an intense peak at 564 cm⁻¹ due to the Fe-O stretching. This peak is characteristic for all spinels and for ferrite structures in particular. Fe₃O₄@SiO₂, on the other hand, also displays a band at 1082 cm⁻¹, which is attributed to Si-O-Si anti-asymmetric stretching vibrations [31], and a broad peak at 3439 cm⁻¹, which corresponds to the O-H stretching. The band at 564 cm⁻¹ corresponds to the Fe-O stretching of the Fe₃O₄ core [50]. The FTIR of MoO₃ shows three peaks below 1000 cm⁻¹, i.e., at 570, 808, and 880 cm⁻¹ corresponding to the stretching modes of oxygen, Mo-O-Mo, and Mo=O, respectively. The characteristic peak at 1405 cm⁻¹ corresponds to the streching of the Mo-OH bond [26,51], and the absorption band at 3182 cm⁻¹ is associated with O-H stretching of surface bound hydroxyls. For FSM, the spectrum clearly indicates MoO₃ has been incorporated in the Fe₃O₄@SiO₂ system as additional peaks at ca. 3182, 882, and 810 cm⁻¹ are observed. Furthermore, a small peak at around 1600 cm⁻¹ (v_{C=C}) can be observed due to the presence of polydopamine, also used in this preparation step.

The various functional groups present in GO were also confirmed by FTIR. The peaks at 1730, 1625, and 1052 cm⁻¹ were assigned to stretching modes of C=O of carboxyl groups, C=C of aromatic groups, and C-O of epoxide groups, respectively. The main absorption peak at 3385 cm⁻¹ corresponds to O-H stretching vibrations. The presence of these functional groups supports that GO was synthesized successfully [52]. These functional groups present on the surface of GO are responsible for its removal capabilities due to the hydrogen bond and π - π interactions, as reported in previous studies [29,47,49,53]. Finally, the functional groups in the optimized FSM-GO (vide infra) absorbing at 3385, 1615, and 1072 cm⁻¹ can be assigned to O-H stretching of hydroxyl, C=O stretching of carboxyl, and C-O stretching of epoxy groups, respectively, all associated to GO [54]. Additional peaks at 818 and 881 cm⁻¹, assigned to Mo=O asymmetric stretching modes of terminal oxygen [55], indicate the existence of a layered orthorhombic MoO₃ phase [56], however, those bands have been shifted in the FSM-GO composite when comparing to MoO₃, demonstrating the formation of chemical bonds between Mo-O and graphene oxide. Furthermore, the Fe-O stretching (v = 573 cm⁻¹) and the Si-O-Si antiasymmetric stretching vibrations ($v_{O-Si-O} = 1074 \text{ cm}^{-1}$) can also be observed in the spectrum, with a small shift. However, the stretching $v_{C=C}$ from the polydopamine cannot be observed due to the overlap with the GO contribution. These results validate the coupling of GO, MoO₃ and Fe₃O₄@SiO₂ in the presence of polydopamine.

481

482

483

484

485

486

487

488

489

490

491

492

493

494

495

496

497

498

499

500

501

502

503

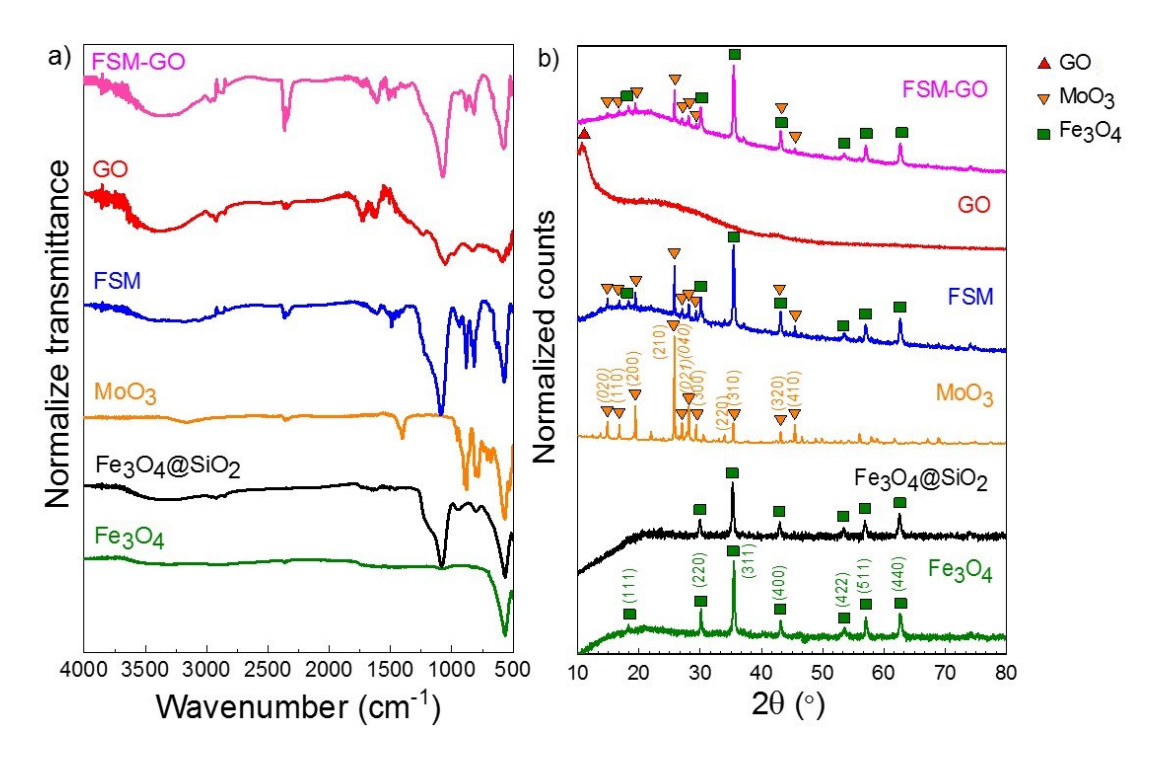


Figure 2. (a) FTIR spectra and (b) XRD patterns of all the components (indicated) involved in the preparation of the FSM-GO catalyst with optimized composition as per RSM methodology. The italicized miller indeces corresponds to h-MoO₃.

All materials were analysed by powder XRD (Figure 2b). The Fe₃O₄ XRD pattern can be indexed to the standard phase of the cubic spinel structure of Fe₃O₄ (JCPDS 19-0629) while no other peaks were observed [57]. The Fe₃O₄@SiO₂ did not present any characteristic SiO₂ peaks, indicating the possible formation of an amorphous SiO₂ phase. The MoO₃ XRD pattern shows strong diffraction peaks corresponding to a highly crystalline mixture of *h*- and α- phases, i.e., of orthorhombic (JCPDS 35-0569) and hexagonal MoO₃ (JCPDS 21-0569) [58]. The FSM pattern presents a combination of the Fe₃O₄ and MoO₃ phases due to the presence of these individual crystalline

components. GO shows a strong (001) peak at 12° associated with the interlayer spacing between graphene sheets. Graphite diffraction peaks (002) were not found, indicating delamination was complete [59]. FSM and FSM@GO showed the similar diffraction patterns, as expected. The GO nanosheets in the nanocomposite remained disordered since no addition diffraction peaks appeared upon GO addition [60].

Raman spectra of GO and FSM-GO (Figure S4) showed D and G bands at 1332 and 1585 cm⁻¹, respectively. The D band provides information to the C sp^3 and the G band to the C sp^2 . The intensity ratio of the D band to the G band (R = I_D/I_G) usually reflects defects in GO and graphene. [61] The R ratio of GO and FSM-GO samples showed an increased ratio from r=0.93 to 1.03, respectively. When GO nanosheets are functionalized with FSM nanoparticles, an increase in the oxygen-functional groups on GO during the reaction takes place. This increase is correlated with a decrease in the size of the sp^2 domains.[62]

SEM images also demonstrated successful synthesis and coupling of the nanomaterials (Figure 3). The SEM image of Fe₃O₄ (Figure 3a) shows particles with irregular to flat plate morphologies. Fe₃O₄@SiO₂ exhibits the morphological properties of Fe₃O₄ (Figure 3b); however, the composite exhibited a smoother surface and slightly larger average particle size. It can be inferred that silica shells uniformly coated the Fe₃O₄ particles and formed Fe₃O₄@SiO₂, as previously shown for Fe₃O₄ nanoparticles coated by the Stöber method [30,31]. SEM images of MoO₃ (Figure 3c) present hexagonal rods of *ca*. 1 μm diameter as well as a smaller fraction of plates with particle thickness of about 100–200 nm arranged in stacking patterns; this is consistent with the formation of *h*- and α-MoO₃ phases as found by XRD. The morphology of

FSM (Figure 3d) exhibits the addition of smaller spherical Fe₃O₄@SiO₂ particles onto anisotropic structures, which likely indicates the coating of the rod-like structured MoO₃ surface by a fraction of the Fe₃O₄@SiO₂ particles and confirm the successful binding of these particles. The SEM image of GO (Figure 3e) displays a nanosheet-like morphology with high flexibility. Randomly aggregated and crumpled thin sheets can be clearly seen in the image. These sheets make GO an ideal nanomaterial to attach different nanoparticles and macromolecules, and allow the incorporation of an extensive variety of chemical functionalizations [63,64]. Finally, the FSM–GO image (Figure 3f) verifies the FSM loading on the GO by the presence of tiny particles attached to the GO sheet. The loading of the catalyst on the GO surface is improved by the interaction of the GO functional groups with the surface of the MoO₃ semiconductor catalyst [8].

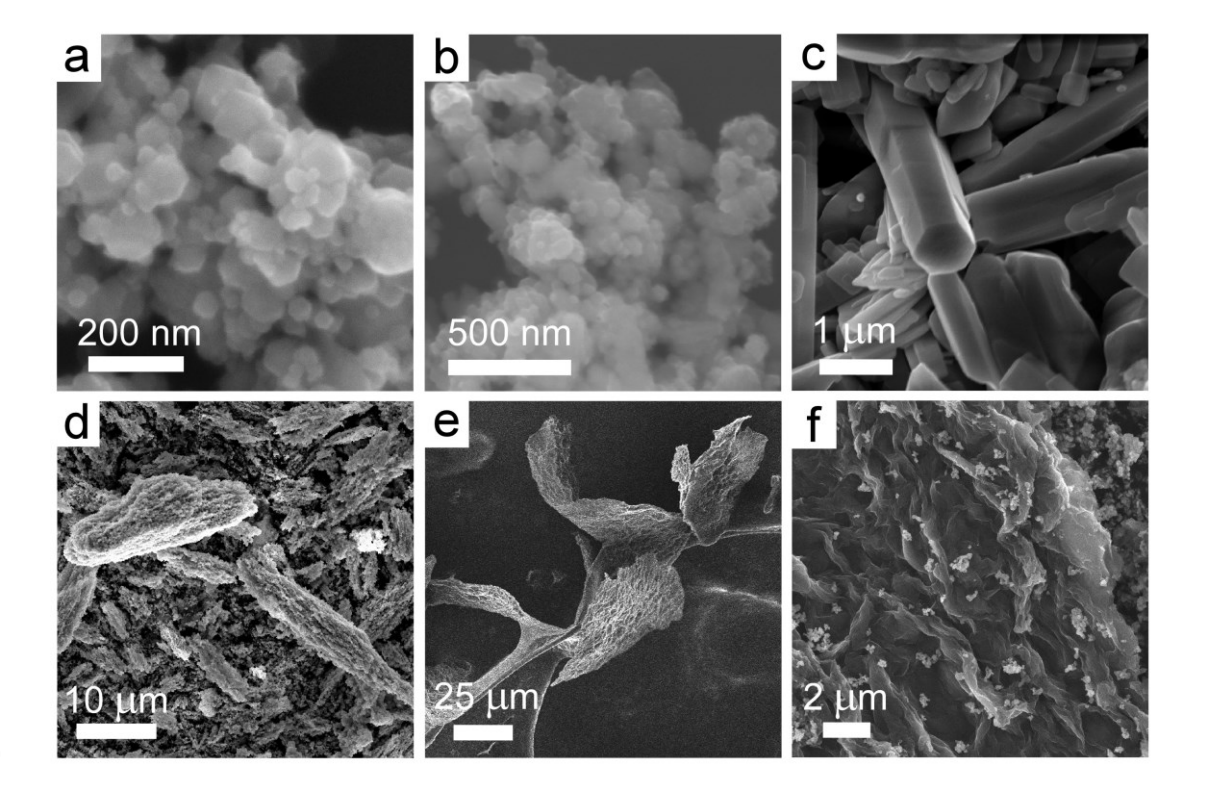


Figure 3. SEM images of (a) Fe₃O₄, (b) Fe₃O₄@SiO₂, (c) MoO₃, (d) FSM, (e) GO, and (f) FSM-GO.

562

563

564

565

566

567

568

569

570

571

572

573

574

575

576

577

578

579

580

581

582

583

584

560

561

Energy dispersive spectroscopy (EDS) was employed to qualitatively evaluate the elemental composition of the optimized sample (Figure S5). Characteristic peaks of Fe (L\alpha 0.7048 eV, K\alpha 6.3996 eV, K\beta 7.058 eV), Si (Kα 1.7398 eV), Mo (Lα 2.2932 eV, Lβ 2,394.81 eV), C (Kα 0.2774 eV), N (K α 0.3924 eV), and O (K α 0.5249 eV) confirm the incorporation of Fe₃O₄@SiO₂, MoO₃ and polydopamine into the composite, respectively. The weak Cl signal (Kα 2.6219 eV) can be attributed to chloride impurities entrapped in the polydopamine matrix polymerized from the D-HCl precursor. The bandgap energies of MoO₃ and FSM-GO, extracted from reflectance measurements (Figure S6) and a Tauc plot (Figure S7), respectively, are presented in Table 1. The bandgap of FSM-GO was estimated to be 2.65 eV, which is slightly lower compared to pure MoO₃, which is typically around 3.05 eV [35,65]. As a result, in the photo-response range, the efficient utilization of visible light spectrum was improved by adding GO into the nanocomposite. Similar findings were reported when GO was incorporated into TiO₂ [66–68]. Finally, the stability of the FSM-GO nanocomposite towards dissolution was studied by measuring the dissolved Mo by atomic absorption spectroscopy (AAS). In a previous publication [26], it was demonstrated that different MoO₃ nanostructures exhibit pH and morphology dependent dissolution behaviours. It has been proven that MoO₃ nanostructures can be dissolved by ca. 30 % in 24

h. The dissolution of Mo in the final nanocomposite (FSM-GO) was evaluated

at pH 5 and 7 for 24 h, finding concentrations of dissolved Mo equal to 0.47 and 0.55 mg/L, respectively (Table 1). Considering the 20 wt% of MoO₃ in the optimized nanocomposite, these low values indicate that very little dissolution of MoO₃ is comparatively observed. The inhibition of the dissolution can be explained by to the presence of a Fe₃O₄-SiO₂-polydopamine coating. This synthetic strategy stabilizes the MoO₃ nanostructure, making this nanomaterial better suitable for water treatment applications.

Table 1. Band-gap energy and dissolution tests of the Mo containing nanomaterials.

Nanomaterial	Energy	Mo	
	bandgap	dissolution	
	(eV)	(mg/L)	
MoO ₃	2.95	100 [26]	
FSM-GO		0.47	
(pH=5)	2.65		
FSM-GO	2.65	0.55	
(pH=7)			

4.4 Effect of batch photocatalysis parameters on MB removal. The photocatalytic MB removal at different FSM-GO loadings between 50 and 250 ppm *vs.* time was investigated as shown in Figure S8. When increasing the FSM-GO concentration, the MB removal increased up to 95 %, reaching a plateau at 200 mg/L. After 60 min, 18.7, 44.0, 69.0, 98.0, and 99.0 % MB removals were achieved for FSM-GO loadings of 50, 100, 150, 200, and 250 mg/L, respectively. From these

results, it was established that the optimum FSM-GO loading is 200 mg/L and the optimum degradation time is 60 min.

602

603

604

605

606

607

608

609

610

611

612

613

614

615

616

617

618

619

620

621

622

623

624

625

Figure S8b shows the removal of MB as a function of the initial MB concentration ([MB]_i). The % MB removal is almost constant at a level of 95% for $[MB]_i \le 40$ ppm, when using 200 mg/L of FSM-GO. However, higher $[MB]_i$ resulted in a decrease in MB removal to 72 % at $[MB]_i = 60$ ppm. At lower [MB]_I, there are enough active sites and light penetration. At higher [MB]_i, fewer active sites are illuminated on the surface of the catalysis. Thus, more competition for active sites happens and removal would take longer [2]. The pH highly influences the removal efficiency since it directly affects the photoefficiency of the photocatalysts. At different pHs, the surface characteristics and the size of aggregated nanoparticles may change affecting adsorption capacity of molecules onto the surface of the nanoparticles [69]. Figure S8c shows the effect of the solution pH on the removal of MB, studied with the optimized FSM-GO formulation. The optimum pH value for MB removal was found to be pH \geq 5, whereas at pH 3 only 35 % MB was removed after 60 min. Previous MB degradation studies reported that there is an increase in the production of reactive oxygen species with increasing pH, which is in agreement with a previously published report [26].

The removal of MB using different visible light sources is presented in Figure 4d. After 60 min, almost 100 % MB removal was achieved for both fluorescent and LED lamps, both having similar relative emission spectra, as shown in Figure S1. Our results indicate that MB removal using FSM–GO is possible within 60 min independently of the visible light source used.

Once the reaction conditions were optimized to achieve the highest MB removal, *i.e.*, at pH 5, 200 mg/L FSM-GO, $[MB]_i = 40$ mg/L MB, under illumination for 60 min, the photocatalytic properties were evaluated for all the materials and the nanocomposite to estimate their relative contribution to the MB removal process (Figure 4). The removal by the optimized FSM-GO composite was higher than those of all control nanomaterials (including GO and MoO₃). While MoO₃ showed ca. 10% MB removal, GO exhibited 40%. Moreover, Fe₃O₄ and Fe₃O₄@SiO₂ exhibited little to negligible discoloration. Furthermore, the effect of the lamp showed no affect on MB degradation (Figure 4). These results suggest that combining GO and MoO₃ produces a more efficient material for MB removal, confirming a synergistic effect between the semiconducting photocatalyst (MoO₃) and the GO light absorption (and adsorption) enhancer.

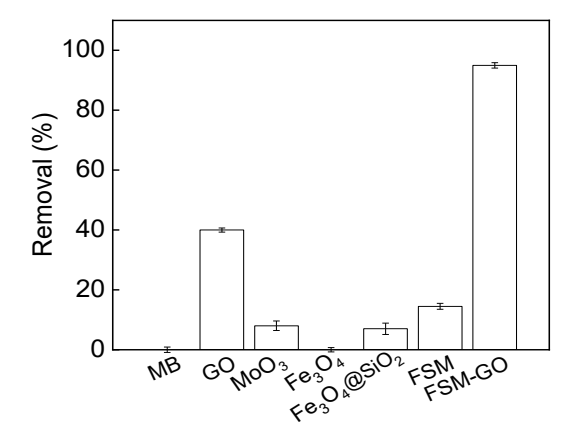


Figure 4. MB removal by GO, MoO₃, Fe₃O₄, Fe₃O₄@SiO₂, and FSM-GO under optimized reaction conditions (40 mg/L MB, 200 mg/L sample, 60 min at pH 5). Error bars represent standard desviations. MB in absence of added sample was used as a control.

The MB removal performance of the FSM-GO composite is higher than for other previously reported materials, as is shown in Table 2. Different catalysts have been reported to have a removal efficiency of around 100% by using lower [MB]_i. However, in our study, we increase the [MB]_i up to 40 ppm, showing an MB removal of almost 100%. Our results indicate that the new FSM-GO nanocomposite could be an alternative for the degradation of MB.

Table 2. Efficiencies of various reported photocatalyst towards MB removal.

Photocatalyst	[MB] _i (mg/L)	Removal efficiency	Ref.
SiO ₂ @α-Fe ₂ O ₃	5	100% after 100 min	[70]
deposited on SnS ₂	3	100% after 100 min	[70]
ZnO-SnO ₂	20	96.53% after 60 min	[71]
TiO ₂ /diatomite	35	100% after 40 min	[72]
Pc-TiO ₂	3	100% after 140 min	[73]
CuPc-TiO ₂	3	100% after 100 min	[74]
			present
FSM-GO	40	99% after 60 min	study

4.5. Reactive oxygen species production. The production of reactive oxygen species(ROS) has been shown to play an important role in photocatalytic reactions. [75]

[76,77] Scavenger experiments were performed to better understand the degradation mechanism of the FSM-GO nanocomposite via generated ROS during reaction. The

production of ROS was evaluated in the presence of isopropyl alcohol (IPA),

triethanolamine (TEOA), and p-benzoquinone (p-BQ), reagents that are well-known to act as scavengers of HO \cdot , h^+ , and O_2^{\cdot} radicals, respectively [23,78–80]. Thus, the MB removal was evaluated upon addition of these scavengers (Figure 6).

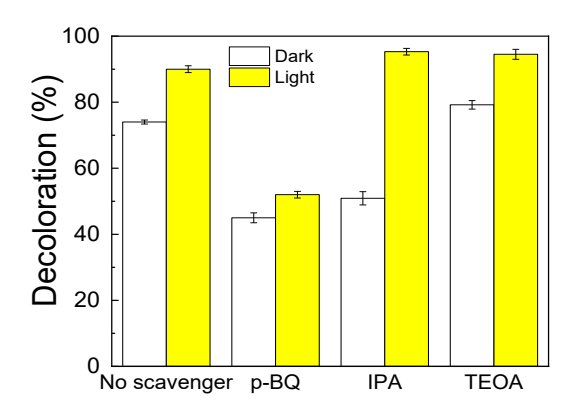


Figure 5. MB removal in the presence of various scavengers in light and dark conditions. Reaction conditions: 40 ppm MB, 200 mg/L FSM-GO, 60 min at pH 5 in the presence of 10 mM TEOA, 75 mM IPA, and 1 mM p-BQ.

The greatest effect was observed with the addition of p-BQ (Figure 5), which is an O_2 scavenger, followed by TEOA, and IPA, indicating that the production of O_2 radical plays an important role in the MB degradation. IPA and TEOA had lower effects on the MB removal, suggesting a less relevant role of HO \cdot and h^+ species. The addition of p-BQ also showed some removal in dark conditions. This MB removal can be due to the MB adsorption on the surface of the composite catalyst. We can confirm that the main MB degradation pathway is via O_2 radicals, which forms via the oxidation of water molecules.

The production of O_2^- involves an electron transfer process where its self-combination (equation 13) results in the H_2O_2 formation [81][76]. Here, we evaluate the production of H_2O_2 to understand the differences in the photocatalytic

properties in light and dark conditions. Figure 6 presents the production of H₂O₂ ROS by measuring the loss of glutathione (GSH) after 1 h in presence of 200 mg/L of each nanomaterial. All nanomaterials produced H₂O₂ showing a considerable difference between light and dark conditions. The differences found for FSM-GO showed that in the presence of light, the production of H₂O₂ increased to *ca.* 60%, compared to the dark, which was only 12 %.

Therefore, we propose that the MB degradation by FSM-GO occurrs according to the equations 11-14, where first MB is adsorbed onto the catalysts surface and then, in the presence of light, the eletrons in the FSM-GO conduction band react with dissolved oxygen to produce O_2 - radical. These generated radicals usually react with a dye followed by the formation of several intermediates, which finally degrades the dye. In the absence of MB, those radicals can recombinate, to form H_2O_2 , as shown in equation 13 [81][76], indicating that the superoxide radical is the main species responsible for the MB degradation .

693
$$FSM - GO + h\nu \rightarrow e^- + h^+$$
 (11)

694
$$O_2 + e^- \rightarrow O_2^{-}$$
 (12)

695
$$O_2^{-} + 2H^+ + e^- \rightarrow H_2O_2$$
 (13)

696 MB +
$$O_2^{-}$$
 \rightarrow Further degradation (14)

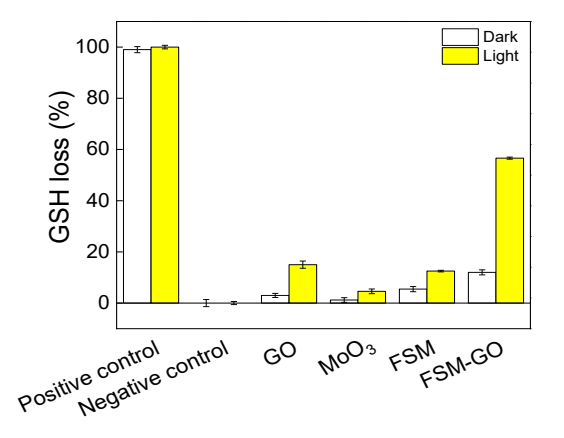


Figure 6. Reactive oxygen species (ROS) activity of H₂O₂ for all the nanomaterials at 200 mg/L after 1 h, expressed as % loss of glutathione (GSH). Positive controls were prepared with the presence of H₂O₂ and negative controls without catalyst. Error bars represent standard deviations.

4.6. Reusability.

In general, materials for contaminant removal should be stable, efficient, cost-effective, and reusable. After the efficiency of this novel FSM-GO composite in removing MB was proven, its reusability was evaluated (Figure 7). After the second cycle, a loss of efficiency in MB removal from 98 % to 85 % was observed. However, a significant reduction in MB removal further took place after the third cycle. This is likely due to the insufficient desorption of MB between cycles, which limited the adsorption of fresh MB on the composite surface

Furthermore, the removal efficiency of the FSM-GO might have been reduced due to the photodegradation of the graphene oxide during the photocatalytic process. [82] These results suggest this composite can only be used for two successive cycles, unless further stabilization and alternative cleaning procedures are developed.

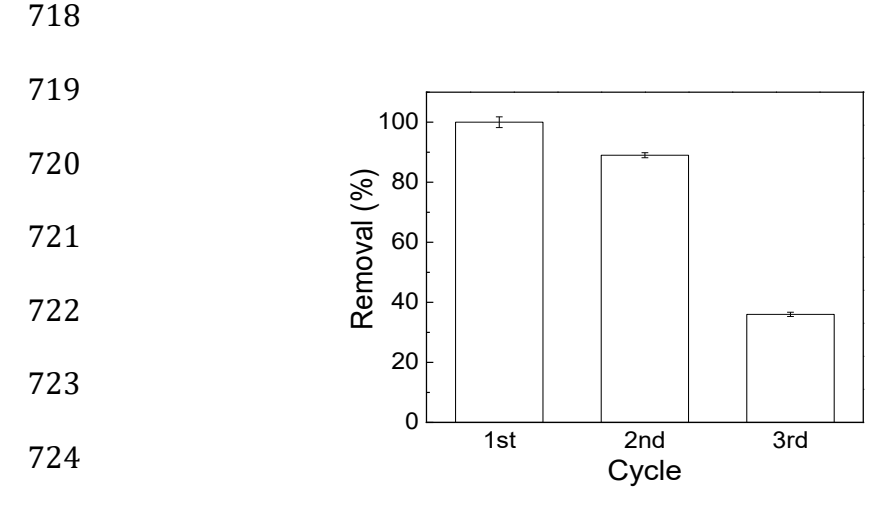


Figure 7. Reusability of FSM-GO at 200 mg/L dose and 40 ppm of MB, 60 min at pH 5. Error bars represent standard deviations.

4.5 Phenol degradation by FSM-GO. Phenol and phenolic substances are widely used in many industries. However, during the last decades, these organic compounds have received increased attention because of their toxicity even at low concentrations and their prevalence in industrial processes. Therefore, phenol is generally evaluated as a model compound in environmental catalysis studies. Figure 8 shows the removal percentage of phenol in the absence and presence of H₂O₂ after 6 h. The photochemical oxidation of phenol and other organic compounds [83–87] with TiO₂, bismute catalysts, and iron phthalocyanine-graphene with the addition of H₂O₂ under UV [83–88] and visible light [89–91] have also been reported. After an hour of adsorption equilibration under dark, followed by 6 h under illumination, 17 % of phenol degradation was achieved. However, by adding 20 μL of H₂O₂ an increase to 85 % of phenol degradation was achieved.

From our results, we need to point out that not only the addition of H_2O_2 is an important factor in the phenol removal, but also the illumination of the

sample plays an significant role since under light, FSM-GO can degrade 85 % of phenol compared to only 17 % under dark conditions. The positive effect of the H₂O₂ addition illustrates the fact that H₂O₂ is a stronger one-electron oxidant than O₂ [92]. The possible photocatalytic mechanism involved is suggested as follows (equation 14-17);

749
$$FSM - GO + hv \rightarrow e^- + h^+$$
 (15)

750
$$e^- + H_2O_2 \rightarrow HO \cdot + OH^-$$
 (16)

$$751 h^+ + OH^- \rightarrow HO (17)$$

752
$$R - OH + HO \rightarrow R + H_2O \rightarrow further oxidation$$
 (18)

Under illumination, if the light energy is equivalent to or greater than the bandgap of the catalyst, electrons in the valence band can be excited to the conduction band creating an electron-hole pair. The electron is then responsible for the oxidation of H_2O_2 to form $HO \cdot$ and OH^- (eq. 16), and the hole is responsible for the reduction of OH^- forming the hydroxyl radical ($HO \cdot$) (eq. 17). Then, those radicals are capable of degrading phenol. It has been proven that the presence of H_2O_2 at the beginning of the reaction further generates hydroxyl radicals. Without the presence of H_2O_2 , hydroxyl radicals may likely react with holes reducing the probability of electron-hole recombination (equation 17) [88].

The difference found between dark and light can be responsible for the degradation of phenol shown in Figure 8 and explained by equations (15–18). These results provide further evidence that the degradation of phenol increases with the addition of H_2O_2 at the beginning of the reaction. Hence, the novel

photocatalyst, FSM-GO, can also be used for the removal of phenol, suggesting that the addition of H_2O_2 and illumination are necessary to achieve high phenol removals.

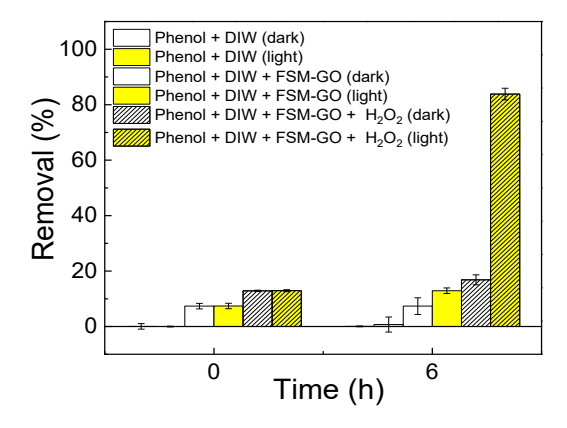


Figure 8. Degradation of phenol in the absence and presence of 20 μ L of 30 wt% H₂O₂ (1000 mg/L FSM-GO, [phenol]_i = 20 ppm, pH = 5). Error bars represent standard deviations.

5. Conclusions

The multifunctional magnetic composite nanomaterial FSM-GO was successfully synthesized and optimized using RSM to effectively remove organic compounds. The statistical analysis showed a good correlation between predicted and experimental responses. Adsorption and photocatalysis exhibited high R^2 values of 0.84 and 0.94, respectively. The characterization of the optimized FSM-GO results confirmed the formation of a novel nanocomposite that is highly stable at pH values of 7 and 5 for photocatalytic applications presenting less Mo loss compared to the MoO₃ nanostructures alone. FTIR measurements showed that the surface of the nanomaterial exhibits diverse functional groups. These functional groups help in the degradation mechanisms, and the reduction of the energy bandgap increases the harvesting

efficiency in the visible light range. This study also demonstrates that the degradation of MB is influenced by various operating parameters, such as pH, dosage, and $[MB]_i$. A degradation efficiency of 99.2 % was obtained with optimized operating values, i.e., contact time of 60 min, 200 mg FSM-GO/L, $[MB]_i = 40$ ppm and pH = 5. Furthermore, we also proved that the FSM-GO nanocomposite can be used in phenol degradation showing that the addition of H₂O₂ under light exposition achieved 85 % of phenol degradation.

Conflicts of interest

- On behalf of all authors, the corresponding author states that there is no conflict
- 796 of interest.

794

797

804

Acknowledgements

- 798 This work was supported by the following funds: Engineering Research and
- 799 Development for Technology (ERDT) Program of the College of Engineering,
- University of the Philippines, Diliman. The NSF BEINM Grant Number: 1705511,
- and the Welch foundation award number (E-2011-20190330). The findings achieved
- herein are solely the responsibility of the authors. We would like to acknowledge Dr.
- Jiming Bao's group, especially Tian Tong, for the Raman measurements.

References

- 805 [1] Y. Yan, Q. Liu, X. Du, J. Qian, H. Mao, K. Wang, Visible light
- photoelectrochemical sensor for ultrasensitive determination of dopamine
- based on synergistic effect of graphene quantum dots and TiO2 nanoparticles,
- 808 Anal. Chim. Acta. 853 (2015) 258–264.
- doi:https://doi.org/10.1016/j.aca.2014.10.021.

- 810 [2] P. Chowdhury, J. Moreira, H. Gomaa, A.K. Ray, Visible-solar-light-driven
- photocatalytic degradation of phenol with dye-sensitized TiO2: parametric and
- kinetic study, Ind. Eng. Chem. Res. 51 (2012) 4523–4532.
- 813 [3] M.M. Haque, M. Muneer, TiO2-mediated photocatalytic degradation of a
- 814 textile dye derivative, bromothymol blue, in aqueous suspensions, Dye.
- Pigment. 75 (2007) 443–448.
- 816 [4] M. Qamar, M. Saquib, M. Muneer, Semiconductor-mediated photocatalytic
- degradation of anazo dye, chrysoidine Y in aqueous suspensions, Desalination.
- 818 171 (2005) 185–193.
- 819 [5] D. Jiang, Y. Xu, D. Wu, Y. Sun, Visible-light responsive dye-modified TiO2
- photocatalyst, J. Solid State Chem. 181 (2008) 593–602.
- 821 [6] S.N. Frank, A.J. Bard, Heterogeneous photocatalytic oxidation of cyanide and
- sulfite in aqueous solutions at semiconductor powders, J. Phys. Chem. 81
- 823 (1977) 1484–1488.
- 824 [7] Y. Tang, G. Zhang, C. Liu, S. Luo, X. Xu, L. Chen, B. Wang, Magnetic TiO2-
- graphene composite as a high-performance and recyclable platform for
- efficient photocatalytic removal of herbicides from water, J. Hazard. Mater.
- 827 252 (2013) 115–122.
- 828 [8] G. Malekshoar, K. Pal, Q. He, A. Yu, A.K. Ray, Enhanced solar photocatalytic
- degradation of phenol with coupled graphene-based titanium dioxide and zinc
- oxide, Ind. Eng. Chem. Res. 53 (2014) 18824–18832.
- 831 [9] F. Zhang, Y. Li, J. Li, Z. Tang, Y. Xu, 3D graphene-based gel photocatalysts
- for environmental pollutants, Environ. Pollut. 253 (2019) 365–376.
- doi:10.1016/j.envpol.2019.06.089.
- 834 [10] N. Zhang, M. Yang, S. Liu, Y. Sun, Y. Xu, Waltzing with the Versatile

- Platform of Graphene to Synthesize Composite Photocatalysts, (2015).
- doi:10.1021/acs.chemrev.5b00267.
- 837 [11] M.-Q. Yang, N. Zhang, M. Pagliaro, Y.-J. Xu, Artificial photosynthesis over
- graphene–semiconductor composites. Are we getting better?, Chem. Soc. Rev.
- 43 (2014) 8240–8254. doi:10.1039/C4CS00213J.
- 840 [12] N. Zhang, Y. Zhang, Y.-J. Xu, Recent progress on graphene-based
- photocatalysts: current status and future perspectives, Nanoscale. 4 (2012)
- 842 5792–5813. doi:10.1039/C2NR31480K.
- 843 [13] T. Graphene, T. Different, TiO 2 . Graphene Nanocomposites for Gas-Phase
- Photocatalytic Degradation of Volatile Aromatic Pollutant: Is, 4 (2010) 7303–
- 845 7314. doi:10.1021/nn1024219.
- 846 [14] O. Akhavan, E. Ghaderi, Photocatalytic Reduction of Graphene Oxide
- Nanosheets on TiO 2 Thin Film for Photoinactivation of Bacteria in Solar
- Light Irradiation, (2009) 20214–20220. doi:10.1021/jp906325q.
- 849 [15] A. Wei, J. Wang, Q. Long, X. Liu, X. Li, X. Dong, W. Huang, Synthesis of
- high-performance graphene nanosheets by thermal reduction of graphene
- 851 oxide, Mater. Res. Bull. 46 (2011) 2131–2134.
- 852 [16] Z.-S. Wu, W. Ren, L. Gao, B. Liu, C. Jiang, H.-M. Cheng, Synthesis of high-
- quality graphene with a pre-determined number of layers, Carbon N. Y. 47
- 854 (2009) 493–499.
- 855 [17] B. Li, T. Liu, Y. Wang, Z. Wang, Journal of Colloid and Interface Science ZnO
- graphene-oxide nanocomposite with remarkably enhanced visible-light-driven
- photocatalytic performance, 377 (2012) 114–121.
- 858 doi:10.1016/j.jcis.2012.03.060.
- 859 [18] Z. Mengting, T. Agustiono, S. Fei, T. Ouyang, M. Ha, D. Othman, M.

- Rezakazemi, S. Shirazian, Applicability of BaTiO 3 / graphene oxide (GO)
- composite for enhanced photodegradation of methylene blue (MB) in
- synthetic wastewater under UV e vis irradiation *, 255 (2019).
- doi:10.1016/j.envpol.2019.113182.
- 864 [19] Y. Li, Q. Du, T. Liu, X. Peng, J. Wang, J. Sun, Y. Wang, S. Wu, Z. Wang, Y.
- Xia, L. Xia, Chemical Engineering Research and Design Comparative study of
- methylene blue dye adsorption onto activated carbon, graphene oxide, and
- 867 carbon nanotubes, Chem. Eng. Res. Des. 91 (2012) 361–368.
- doi:10.1016/j.cherd.2012.07.007.
- 869 [20] J. Peña-Bahamonde, C. Wu, S.K. Fanourakis, S.M. Louie, J. Bao, D.F.
- 870 Rodrigues, Oxidation state of Mo affects dissolution and visible-light
- photocatalytic activity of MoO3 nanostructures, J. Catal. 381 (2020) 508–519.
- 872 [21] G.P. Nagabhushana, D. Samrat, G.T. Chandrappa, α-MoO ₃ nanoparticles:
- solution combustion synthesis, photocatalytic and electrochemical properties,
- 874 RSC Adv. 4 (2014) 56784–56790. doi:10.1039/C4RA05135A.
- 875 [22] Y. Chen, C. Lu, L. Xu, Y. Ma, W. Hou, J.-J. Zhu, Single-crystalline
- orthorhombic molybdenum oxide nanobelts: synthesis and photocatalytic
- properties, CrystEngComm. 12 (2010) 3740. doi:10.1039/c000744g.
- 878 [23] a. Chithambararaj, N.S. Sanjini, a. C. Bose, S. Velmathi, Flower-like
- hierarchical h-MoO3: new findings of efficient visible light driven nano
- photocatalyst for methylene blue degradation, Catal. Sci. Technol. 3 (2013)
- 881 1405. doi:10.1039/c3cy20764a.
- 882 [24] S.K. Misra, A. Dybowska, D. Berhanu, S.N. Luoma, E. Valsami-Jones, The
- complexity of nanoparticle dissolution and its importance in nanotoxicological
- 884 studies, Sci. Total Environ. 438 (2012) 225–232.

- doi:10.1016/j.scitotenv.2012.08.066.
- 886 [25] S.K. Fanourakis, J. Peña-Bahamonde, D.F. Rodrigues, Inorganic salts and
- organic matter effects on nanorod{,} nanowire{,} and nanoplate MoO3
- aggregation {,} dissolution {,} and photocatalysis, Environ. Sci. Nano. (2020).
- doi:10.1039/D0EN00708K.
- 890 [26] J. Peña-bahamonde, C. Wu, S.K. Fanourakis, S.M. Louie, J. Bao, D.F.
- Rodrigues, Oxidation state of Mo affects dissolution and visible-light
- photocatalytic activity of MoO 3 nanostructures, 381 (2020) 508-519.
- 893 doi:10.1016/j.jcat.2019.11.035.
- 894 [27] M.N. Braimah, A.N. Anozie, O.J. Odejobi, Utilization of Response sUrface
- Methodology (RSM) in the Optimization of Crude Oil Refinery Process, New
- Port-Harcourt Refinery, Nigeria, J. Eng. Sci. Technol. 3 (2016) 4361–4369.
- 897 [28] A. Witek-Krowiak, K. Chojnacka, D. Podstawczyk, A. Dawiec, K. Pokomeda,
- Application of response surface methodology and artificial neural network
- methods in modelling and optimization of biosorption process, Bioresour.
- 900 Technol. 160 (2014) 150–160.
- 901 [29] J.V.D. Perez, E.T. Nadres, H.N. Nguyen, M.L.P. Dalida, D.F. Rodrigues,
- Response surface methodology as a powerful tool to optimize the synthesis of
- 903 polymer-based graphene oxide nanocomposites for simultaneous removal of
- 904 cationic and anionic heavy metal contaminants, RSC Adv. 7 (2017) 18480-
- 905 18490. doi:10.1039/C7RA00750G.
- 906 [30] W. Stöber, A. Fink, E. Bohn, Controlled growth of monodisperse silica spheres
- in the micron size range, J. Colloid Interface Sci. 26 (1968) 62–69.
- 908 [31] R. Karimi-Chayjani, N. Daneshvar, M.S.N. Langarudi, F. Shirini, H. Tajik,
- 909 Silica-coated magnetic nanoparticles containing bis dicationic bridge for the

- 910 synthesis of 1, 2, 4-triazolo pyrimidine/quinazolinone derivatives, J. Mol.
- 911 Struct. 1199 (2020) 126891.
- 912 [32] A. Chithambararaj, N.S. Sanjini, S. Velmathi, A.C. Bose, Preparation of h-
- 913 MoO 3 and α-MoO 3 nanocrystals: comparative study on photocatalytic
- degradation of methylene blue under visible light irradiation, Phys. Chem.
- 915 Chem. Phys. 15 (2013) 14761–14769.
- 916 [33] D.C. Marcano, D. V Kosynkin, J.M. Berlin, A. Sinitskii, Z. Sun, A. Slesarev,
- 917 L.B. Alemany, W. Lu, J.M. Tour, Improved synthesis of graphene oxide, ACS
- 918 Nano. 4 (2010) 4806–4814.
- 919 [34] J. Tauc, OPTICAL PROPERTIES AND ELECTRONIC STRUCTURE OF
- 920 AMORPHOUS Ge AND Si, Mat. Res. Bull. 3 (1968) 37–46.
- 921 [35] A. Chithambararaj, N.S. Sanjini, S. Velmathi, A. Chandra Bose, Preparation of
- 922 h-MoO3 and α-MoO3 nanocrystals: comparative study on photocatalytic
- degradation of methylene blue under visible light irradiation, Phys. Chem.
- 924 Chem. Phys. 15 (2013) 14761–14769. doi:10.1039/C3CP51796A.
- 925 [36] X. Wang, T.-T. Lim, Solvothermal synthesis of C-N codoped TiO2 and
- 926 photocatalytic evaluation for bisphenol A degradation using a visible-light
- 927 irradiated LED photoreactor, Appl. Catal. B Environ. 100 (2010) 355–364.
- 928 [37] S.J. Atherton, A. Harriman, Photochemistry of Intercalated Methylene Blue:
- Photoinduced Hydrogen Atom Abstraction from Guanine and Adenine, (1993)
- 930 1816–1822. doi:10.1021/ja00058a028.
- 931 [38] J. Peña-Bahamonde, V. San Miguel, H.N. Nguyen, R. Ozisik, D.F. Rodrigues,
- J.C. Cabanelas, Functionalization of reduced graphene oxide with polysulfone
- brushes enhance antibacterial properties and reduce human cytotoxicity,
- 934 Carbon N. Y. 111 (2017) 258–268. doi:10.1016/j.carbon.2016.10.005.

- 935 [39] G.L. Ellman, Tissue sulfhydryl groups, Arch. Biochem. Biophys. 82 (1959)
- 936 70–77.
- 937 [40] I.E. Mejías Carpio, C.M. Santos, X. Wei, D.F. Rodrigues, Toxicity of a
- 938 polymer–graphene oxide composite against bacterial planktonic cells, biofilms,
- 939 and mammalian cells, Nanoscale. 4 (2012) 4746. doi:10.1039/c2nr30774j.
- 940 [41] M. Sarkar, P. Majumdar, Application of response surface methodology for
- optimization of heavy metal biosorption using surfactant modified chitosan
- 942 bead, Chem. Eng. J. 175 (2011) 376–387.
- 943 [42] F. Shakeel, N. Haq, F.K. Alanazi, I.A. Alsarra, Box-Behnken statistical design
- for removal of methylene blue from aqueous solution using sodium dodecyl
- sulfate self-microemulsifying systems, Ind. Eng. Chem. Res. 53 (2014) 1179–
- 946 1188.
- 947 [43] I.E. Mejias Carpio, J.D. Mangadlao, H.N. Nguyen, R.C. Advincula, D.F.
- Rodrigues, Graphene oxide functionalized with ethylenediamine triacetic acid
- for heavy metal adsorption and anti-microbial applications, Carbon N. Y. 77
- 950 (2014) 289–301. doi:10.1016/j.carbon.2014.05.032.
- 951 [44] R.P. Medina, E.T. Nadres, F.C. Ballesteros, D.F. Rodrigues, Incorporation of
- graphene oxide into a chitosan-poly (acrylic acid) porous polymer
- 953 nanocomposite for enhanced lead adsorption, Environ. Sci. Nano. 3 (2016)
- 954 638–646.
- 955 [45] S.C. Smith, D.F. Rodrigues, Carbon-based nanomaterials for removal of
- chemical and biological contaminants from water: a review of mechanisms and
- 957 applications, Carbon N. Y. 91 (2015) 122–143.
- 958 [46] Y.L.F. Musico, C.M. Santos, M.L.P. Dalida, D.F. Rodrigues, Improved
- 959 removal of lead(ii) from water using a polymer-based graphene oxide

- 960 nanocomposite, J. Mater. Chem. A. 1 (2013) 3789. doi:10.1039/c3ta01616a.
- 961 [47] P.C. Bandara, E.T. Nadres, D.F. Rodrigues, Use of Response Surface
- Methodology To Develop and Optimize the Composition of a Chitosan-
- Polyethyleneimine-Graphene Oxide Nanocomposite Membrane Coating To
- More Effectively Remove Cr(VI) and Cu(II) from Water, ACS Appl. Mater.
- 965 Interfaces. 11 (2019) 17784–17795. doi:10.1021/acsami.9b03601.
- 966 [48] H. Zhu, Y. Fu, R. Jiang, J. Yao, L. Xiao, G. Zeng, Optimization of copper (II)
- adsorption onto novel magnetic calcium alginate/maghemite hydrogel beads
- using response surface methodology, Ind. Eng. Chem. Res. 53 (2014) 4059–
- 969 4066.
- 970 [49] H. Al-Kandari, A.M. Abdullah, A.M. Mohamed, S. Al-Kandari, Enhanced
- photocatalytic degradation of a phenolic compounds' mixture using a highly
- 972 efficient TiO 2/reduced graphene oxide nanocomposite, J. Mater. Sci. 51
- 973 (2016) 8331–8345.
- 974 [50] M.A. Ghasemzadeh, M.H. Abdollahi-Basir, M. Babaei, Fe3O4@ SiO2-NH2
- ore-shell nanocomposite as an efficient and green catalyst for the multi-
- omponent synthesis of highly substituted chromeno [2, 3-b] pyridines in
- aqueous ethanol media, Green Chem. Lett. Rev. 8 (2015) 40–49.
- 978 [51] M. Dhanasankar, K.K. Purushothaman, G. Muralidharan, Effect of temperature
- of annealing on optical, structural and electrochromic properties of sol-gel dip
- coated molybdenum oxide films, Appl. Surf. Sci. 257 (2011) 2074–2079.
- 981 [52] C.K. Chua, Z. Sofer, M. Pumera, Graphite oxides: effects of permanganate and
- chlorate oxidants on the oxygen composition., Chem. A Eur. J. 18 (2012)
- 983 13453–9. doi:10.1002/chem.201202320.
- 984 [53] P.C. Bandara, E.T. Nadres, J. Peña-Bahamonde, D.F. Rodrigues, Impact of

- water chemistry, shelf-life, and regeneration in the removal of different
- chemical and biological contaminants in water by a model Polymeric Graphene
- Oxide Nanocomposite Membrane Coating, J. Water Process Eng. 32 (2019)
- 988 100967. doi:https://doi.org/10.1016/j.jwpe.2019.100967.
- 989 [54] H. Wang, X. Yuan, Y. Wu, H. Huang, G. Zeng, Y. Liu, X. Wang, N. Lin, Y.
- 990 Qi, Adsorption characteristics and behaviors of graphene oxide for Zn (II)
- removal from aqueous solution, Appl. Surf. Sci. 279 (2013) 432–440.
- 992 [55] T. Siciliano, A. Tepore, E. Filippo, G. Micocci, M. Tepore, Characteristics of
- molybdenum trioxide nanobelts prepared by thermal evaporation technique,
- 994 Mater. Chem. Phys. 114 (2009) 687–691.
- 995 [56] G.S. Zakharova, C. Täschner, V.L. Volkov, I. Hellmann, R. Klingeler, A.
- 996 Leonhardt, B. Büchner, MoO3– δ nanorods: Synthesis, characterization and
- magnetic properties, Solid State Sci. 9 (2007) 1028–1032.
- 998 [57] M. Sundrarajan, M. Ramalakshmi, Novel cubic magnetite nanoparticle
- synthesis using room temperature ionic liquid, J. Chem. 9 (2012) 1070–1076.
- 1000 [58] H. Hu, C. Deng, J. Xu, K. Zhang, M. Sun, Metastable h-MoO3 and stable α-
- MoO3 microstructures: controllable synthesis, growth mechanism and their
- enhanced photocatalytic activity, J. Exp. Nanosci. 10 (2015) 1336–1346.
- 1003 [59] K. Krishnamoorthy, G.-S. Kim, S.J. Kim, Graphene nanosheets: Ultrasound
- assisted synthesis and characterization., Ultrason. Sonochem. 20 (2013) 644–9.
- doi:10.1016/j.ultsonch.2012.09.007.
- 1006 [60] M.Z. Kassaee, E. Motamedi, M. Majdi, Magnetic Fe3O4-graphene
- oxide/polystyrene: Fabrication and characterization of a promising
- 1008 nanocomposite, Chem. Eng. J. 172 (2011) 540–549.
- doi:10.1016/j.cej.2011.05.093.

- 1010 [61] K. Krishnamoorthy, M. Veerapandian, K. Yun, S. Kim, The chemical and
- structural analysis of graphene oxide with different degrees of oxidation,
- 1012 Carbon N. Y. 53 (2012) 38–49. doi:10.1016/j.carbon.2012.10.013.
- 1013 [62] X. Liu, Y. Shi, Y. Dong, H. Li, Y. Xia, H. Wang, of novel W-doped TiO 2
- nanoparticles / reduced graphene oxide composites with enhanced
- photodegradation performance under visible, (2017) 13382–13390.
- 1016 doi:10.1039/c7nj02320k.
- 1017 [63] T. Kuila, S. Bose, A.K. Mishra, P. Khanra, N.H. Kim, J.H. Lee, Chemical
- functionalization of graphene and its applications, Prog. Mater. Sci. 57 (2012)
- 1019 1061–1105. doi:10.1016/j.pmatsci.2012.03.002.
- 1020 [64] F. Perreault, A.F. De Faria, M. Elimelech, Environmental applications of
- graphene-based nanomaterials, Chem. Soc. Rev. 44 (2015) 5861–5896.
- 1022 [65] Y. Zhao, J. Liu, Y. Zhou, Z. Zhang, Y. Xu, HNaramoto, S. Yamamoto,
- Preparation Of MoO3 nanostructures and their optical properties, J. Phys.
- 1024 Condens. Matter · . 15 (2003) 1547–1552. doi:10.1088/0953-8984/15/35/101.
- 1025 [66] H. Saleem, A. Habib, Study of band gap reduction of TiO2 thin films with
- variation in GO contents and use of TiO2/Graphene composite in hybrid solar
- 1027 cell, J. Alloys Compd. 679 (2016) 177–183.
- doi:https://doi.org/10.1016/j.jallcom.2016.03.240.
- 1029 [67] L.-L. Tan, W.-J. Ong, S.-P. Chai, A.R. Mohamed, Noble metal modified
- reduced graphene oxide/TiO2 ternary nanostructures for efficient visible-light-
- driven photoreduction of carbon dioxide into methane, Appl. Catal. B Environ.
- 1032 166–167 (2015) 251–259. doi:https://doi.org/10.1016/j.apcatb.2014.11.035.
- 1033 [68] A.W. Morawski, E. Kusiak-Nejman, A. Wanag, J. Kapica-Kozar, R.J. Wróbel,
- B. Ohtani, M. Aksienionek, L. Lipińska, Photocatalytic degradation of acetic

- acid in the presence of visible light-active TiO2-reduced graphene oxide
- 1036 photocatalysts, Catal. Today. 280 (2017) 108–113.
- doi:https://doi.org/10.1016/j.cattod.2016.05.055.
- 1038 [69] F. Azeez, E. Al-Hetlani, M. Arafa, Y. Abdelmonem, A.A. Nazeer, M.O. Amin,
- M. Madkour, The effect of surface charge on photocatalytic degradation of
- methylene blue dye using chargeable titania nanoparticles, Sci. Rep. 8 (2018)
- 1041 1–9.
- 1042 [70] S. Balu, K. Uma, G.-T. Pan, T.C.-K. Yang, S.K. Ramaraj, Degradation of
- methylene blue dye in the presence of visible light using SiO2@ α-Fe2O3
- nanocomposites deposited on SnS2 flowers, Materials (Basel). 11 (2018) 1030.
- 1045 [71] J. Lin, Z. Luo, J. Liu, P. Li, Photocatalytic degradation of methylene blue in
- aqueous solution by using ZnO-SnO2 nanocomposites, Mater. Sci. Semicond.
- 1047 Process. 87 (2018) 24–31.
- 1048 [72] R. Zuo, G. Du, W. Zhang, L. Liu, Y. Liu, L. Mei, Z. Li, Photocatalytic
- degradation of methylene blue using TiO2 impregnated diatomite, Adv. Mater.
- 1050 Sci. Eng. 2014 (2014).
- 1051 [73] Y. Nosaka, A.Y. Nosaka, Generation and Detection of Reactive Oxygen
- 1052 Species in Photocatalysis, Chem. Rev. 117 (2017) 11302–11336.
- doi:10.1021/acs.chemrev.7b00161.
- 1054 [74] B. Cabir, M. Yurderi, N. Caner, M.S. Agirtas, M. Zahmakiran, M. Kaya,
- Methylene blue photocatalytic degradation under visible light irradiation on
- copper phthalocyanine-sensitized TiO2 nanopowders, Mater. Sci. Eng. B. 224
- 1057 (2017) 9–17.
- 1058 [75] Y. Nosaka, A.Y. Nosaka, Generation and Detection of Reactive Oxygen
- 1059 Species in Photocatalysis, Chem. Rev. 117 (2017) 11302–11336.

- doi:10.1021/acs.chemrev.7b00161.
- 1061 [76] A.S. Adeleye, X. Wang, F. Wang, R. Hao, W. Song, Y. Li, Photoreactivity of
- graphene oxide in aqueous system: Reactive oxygen species formation and
- bisphenol A degradation, Chemosphere. 195 (2018) 344–350.
- doi:10.1016/j.chemosphere.2017.12.095.
- 1065 [77] Y. Li, W. Zhang, J. Niu, Y. Chen, Mechanism of photogenerated reactive
- oxygen species and correlation with the antibacterial properties of engineered
- metal-oxide nanoparticles, ACS Nano. 6 (2012) 5164–5173.
- 1068 doi:10.1021/nn300934k.
- 1069 [78] M. Zhong, Z. Wei, X. Meng, F. Wu, J. Li, From MoS2 microspheres to α-
- MoO3 nanoplates: Growth mechanism and photocatalytic activities, Eur. J.
- 1071 Inorg. Chem. 2014 (2015) 3245–3251. doi:10.1002/ejic.201402079.
- 1072 [79] Z. Liu, Y. Jin, F. Teng, X. Hua, M. Chen, An efficient Ce-doped MoO 3
- catalyst and its photo-thermal catalytic synergetic degradation performance for
- dye pollutant, CATCOM. 66 (2015) 42–45. doi:10.1016/j.catcom.2015.03.017.
- 1075 [80] Y. Liu, P. Feng, Z. Wang, X. Jiao, F. Akhtar, Novel fabrication and enhanced
- photocatalytic MB degradation of hierarchical porous monoliths of MoO3
- Nanoplates, Sci. Rep. 7 (2017). doi:10.1038/s41598-017-02025-3.
- 1078 [81] A.S. Jalilov, C. Zhang, E.L.G. Samuel, W.K.A. Sikkema, G. Wu, V. Berka,
- T.A. Kent, A. Tsai, J.M. Tour, Mechanistic Study of the Conversion of
- Superoxide to Oxygen and Hydrogen Peroxide in Carbon Nanoparticles,
- 1081 (2016). doi:10.1021/acsami.6b03502.
- 1082 [82] O. Akhavan, M. Abdolahad, A. Esfandiar, M. Mohatashamifar,
- 1083 Photodegradation of Graphene Oxide Sheets by TiO 2 Nanoparticles after a
- Photocatalytic Reduction, (2010) 12955–12959. doi:10.1021/jp103472c.

- 1085 [83] A. Dixit, A.K. Mungray, M. Chakraborty, Photochemical oxidation of phenol
- and chlorophenol by UV/H 2 O 2/TiO 2 process: a kinetic study, in: 2010 2nd
- 1087 Int. Conf. Chem. Biol. Environ. Eng., IEEE, 2010: pp. 153–157.
- 1088 [84] M. Bertelli, E. Selli, Reaction paths and efficiency of photocatalysis on TiO2
- and of H2O2 photolysis in the degradation of 2-chlorophenol, J. Hazard. Mater.
- 1090 138 (2006) 46–52.
- 1091 [85] W. Chu, C.C. Wong, The photocatalytic degradation of dicamba in TiO2
- suspensions with the help of hydrogen peroxide by different near UV
- 1093 irradiations, Water Res. 38 (2004) 1037–1043.
- 1094 [86] C.D. Stalikas, L. Lunar, S. Rubio, F. Sciences, A. Chemistry, U. De Cordoba,
- 1095 C. De Rabanales, E.A. C-, H 2 O 2 / TiO 2 photocatalytic oxidation of metol .
- Identification of intermediates and reaction pathways, 36 (2002) 3582–3592.
- 1097 [87] T. Chen, R. Doong, L. Wen-gang, Photocatalytic degradation of parathion in
- aqueous TiO2 dispersion: the effect of hydrogen peroxide and light intensity,
- 1099 Water Sci. Technol. (1998) 187–194.
- 1100 [88] C.-H. Chiou, C.-Y. Wu, R.-S. Juang, Influence of operating parameters on
- photocatalytic degradation of phenol in UV/TiO2 process, Chem. Eng. J. 139
- 1102 (2008) 322–329.
- 1103 [89] J. Sheng, X. Li, Y. Xu, Generation of H2O2 and OH Radicals on Bi2WO6 for
- Phenol Degradation under Visible Light, ACS Catal. 4 (2014) 732–737.
- doi:10.1021/cs400927w.
- 1106 [90] X. Li, C. Chen, J. Zhao, Mechanism of Photodecomposition of H 2 O 2 on TiO
- 1107 2 Surfaces under Visible Light Irradiation, (2001) 4118–4122.
- doi:10.1021/la010035s.
- 1109 [91] Q. Wang, H. Li, J. Yang, Q. Sun, Q. Li, J. Yang, Applied Catalysis B:

1110		Environmenta	ıl Iron ph	thalocya	anine-graphen	e donor	-acceptor h	ybrids f	for
1111		visible-light-a	ssisted deg	gradation	n of phenol	in the p	resence of	Н 2 О	2,
1112		"Applied	Catal.	В,	Environ.	192	(2016)	182–19	€2.
1113		doi:10.1016/j.	apcatb.2010	6.03.047	7.				
1114	[92]	D. Bi, Y. Xu, Improved Photocatalytic Activity of WO3 through Clustered							
1115		Fe2O3 for Organic Degradation in the Presence of H2O2, Langmuir. 27 (2011)							
1116		9359–9366. d	oi:10.1021/	la20127	93.				
1117									
1118									
1119									